

## A Deprojection Analysis of Abell 1650 with *XMM-Newton*\*

Shu-Mei Jia<sup>1,2</sup>, Yong Chen<sup>2</sup> and Li Chen<sup>1</sup>

<sup>1</sup> Department of Astronomy, Beijing Normal University, Beijing 100875; [jiasm@mail.ihep.ac.cn](mailto:jiasm@mail.ihep.ac.cn)

<sup>2</sup> Key Laboratory of Particle Astrophysics, Institute of High Energy Physics, Chinese Academy of Sciences, Beijing 100049

Received 2005 July 20; accepted 2005 September 20

**Abstract** We revisit the *XMM-Newton* observation of the galaxy cluster Abell 1650 with a deprojection technique. We find that the radial deprojected spectra of Abell 1650 can be marginally fitted by a single-temperature model. In order to study the properties of the central gas, we fit the spectra of the central two regions with a two-temperature model. The fits then become significantly better and the cool gas about 1~2 keV can be connected with the gas cooling. Fitting the central spectrum ( $r \leq 1'$ ) by using a cooling flow model with an isothermal component yields a small mass deposition rate of  $10_{-7}^{+11} M_{\odot} \text{ yr}^{-1}$ , while the standard cooling flow model can not fit this spectrum satisfactorily except that there exists a cut-off temperature having a level of about 3 keV. From the isothermal model we derive the deprojected electron density profile  $n_e(r)$ , and then together with the deprojected temperature profile the total mass and gas mass fraction of cluster are also determined. We compare the properties of Abell 1650 with those of Abell 1835 (a large cooling flow cluster) and some other clusters, to explore the difference in properties between large and small cooling flow cluster, and what causes the difference in the cooling flow of different clusters. It has been shown that Abell 1835 has a steeper potential well and thus a higher electron density and a lower temperature in its center, indicating that the shape of the gravitational potential well in central region determines the cooling flow rates of clusters. We calculate the potential, internal and radiated energies of these two clusters, and find that the gas energies in both clusters are conserved during the collapsing stage.

**Key words:** galaxies: clusters: individual: Abell 1650 —galaxies: cooling flows — galaxies: evolution — galaxies: intergalactic medium — X-rays: galaxies: clusters

### 1 INTRODUCTION

Clusters of galaxies are the largest gravitationally bound systems in the universe. Present cluster samples are mainly based on the ASCA and/or ROSAT data (Peres et al. 1998; Markevitch et al. 1998; White 2000; Reiprich & Böhringer 2002; Ikebe et al. 2002; Sanderson et al. 2003). However, despite their similarity, they have generated much controversies: in particular, rather different results in temperature have been found for, e.g., Abell 1650: Sanderson et al. (2003) found  $T = 8.04_{-1.14}^{+1.75}$  keV while Ikebe et al. (2002) found  $T = 5.68_{-0.27}^{+0.30}$  keV. These studies have been hampered somewhat by questions of Point Spread Function (PSF) and sensitivity limits, and discrepancies between different observations as well as between different authors analysing the same

---

\* Supported by the National Natural Science Foundation of China.

observation data, hence we urge for a more careful examination with high quality data. In addition, we should consider the effects of projection and the temperature variation with radius on the clusters' properties such as the mass and luminosity.

Cooling is an important characteristic of clusters, and clusters have been historically divided into two types: cooling flow clusters and non-cooling flow clusters. Then, what causes the different cooling flows? how does cooling affect the properties of a cluster? and does there exist any difference in such properties as the temperature, electron density and gas mass fraction between large and small cooling flow clusters? The prevailing view is that the non-cooling flow clusters are systems that have been disrupted by recent major mergers (e.g., Yuan et al. 2005). This picture is often supported by images of non-cooling flow clusters that show disturbed X-ray morphologies, but there are several non-cooling flow clusters that look remarkably relaxed and do not show any obvious signs of ongoing mergers (e.g., 3C 129, Abell 2589). McCarthy et al. (2004) considered a model of Intrachuster Medium (ICM) with radiative cooling and entropy injection to explain the global and structural properties of clusters, and found that the entropy injection offers a natural way to distinguish between a cooling flow cluster (with mild levels of entropy injection  $\leq 300 \text{ keV cm}^2$ ) and a relaxed non-cooling flow cluster (with a much higher entropy injection).

Abell 1650 is a luminous, medium redshift ( $z = 0.0845$ ) (Abell et al. 1989) cluster of galaxies with a relaxed structure that has appeared in several cluster samples, and thus is an important object to study the above issues. In previous observations, Abell 1650 was found to be a moderate cooling flow cluster with a mass deposition rate of  $\dot{M} = 280_{-89}^{+464} M_{\odot} \text{ yr}^{-1}$  within the cooling flow radius  $165_{-24}^{+103} \text{ kpc}$  (from ROSAT data, Peres et al. 1998) and a total mass  $9.62_{-2.92}^{+4.91} \times 10^{14} M_{\odot}$  within  $r_{500} = 1.88_{-0.21}^{+0.28} \text{ Mpc}$  (from ROSAT and ASCA data, Reiprich & Böhringer 2002). Takahashi & Yamashita (2003) have analyzed the *XMM-Newton* data of Abell 1650 using a projection technique and found that its average temperature within  $5'$  is  $5.62_{-0.07}^{+0.05} \text{ keV}$ . Deprojection can reveal the real spectrum of the cluster gas in different spherical shells, and we can further determine the deprojected temperature and the mass distribution of the gas in the cluster. Here, we revisit the *XMM-Newton* observation of Abell 1650 using a deprojection technique (e.g., Pratt & Arnaud 2002; Chen et al. 2003) to study its X-ray properties, and then compare it with a large cooling flow cluster, Abell 1835 (Jia et al. 2004) and some other clusters, to investigate if there exist any difference in their properties and what causes the cooling flow difference among clusters. These two clusters were analysed by the same deprojection technique to reduce the systematic errors. Now, *XMM-Newton* is the most sensitive X-ray telescope with a high spatial and spectral resolution, and it is most useful for analysis by providing more reliable estimates of the parameters including temperature.

The structure of this paper is as follows: Section 2 describes the observation, background correction and spectral deprojection technique. Section 3 presents the spectral fits with different models and derives the deprojected temperature profile, properties of the central gas and mass deposition rate. In Section 4 we obtain the deprojected electron density profile based on the single-temperature model and then calculate the total mass. In Section 5 we compare the temperature, gravitational potential well, electron density, gas mass fraction, and the internal, potential and radiated energies of gas in Abell 1650 with those of Abell 1835 and some other clusters. Our conclusions are given in Section 6.

Throughout this paper, unless otherwise noted the energy band we selected is 0.5–10 keV, the solar abundance standard used in XSPEC (X-Ray Spectral Fitting Package) is the default one 'angr' (Anders & Grevesse 1989), and the cosmology model is  $H_0 = 100h \text{ km s}^{-1} \text{ Mpc}^{-1}$  where  $h = 0.5$ ,  $q_0 = 0.5$ ,  $\Omega_m = 1.0$ , and  $\Omega_{\Lambda} = 0$ .  $1'$  corresponds to 127.9 kpc at the distance of Abell 1650.

## 2 OBSERVATION AND DATA PREPARATION

Abell 1650 was observed for 43 ks in December 2001 by *XMM-Newton* (observation ID 0093200101). In this paper, only data from the EPIC cameras (MOS1, MOS2 and pn) are considered. The observation was made in the full frame window mode with a medium filter. Throughout this analysis, we only use the event with FLAG=0, PATTERN $\leq 4$  for pn and PATTERN $\leq 12$  for MOS. The calibration is given in SAS (Science Analysis System) 5.4.1.

## 2.1 Background Correction

The light curve given by this observation shows some flares which were caused by the low energy protons produced by solar activity. Since the X-ray flux of the cluster can not change during the observation period, we discard by eye all intervals with prominent flares and select only those intervals with count rates within  $3\sigma$  of the overall average count rate. This gave an effective exposure time 32.7ks for MOS1, 32.6ks for MOS2 and 28.6ks for pn. After the removal of flare intervals, the *XMM-Newton* background is dominated by the following two components:

i) Particle background: high energy particles like cosmic-rays pass through the satellite and deposit a fraction of their energy on the detector. It dominates at high energy and is not affected by the telescope vignetting.

ii) Cosmic X-ray Background (CXB): the CXB varies across the sky (Snowden et al. 1997) and is more important at the low energy. To correct for this background, the vignetting effect must be taken into account.

We used the observation of the ‘Lockman Hole’ (observation ID: 0147511801, hereafter LH) to subtract these two kinds of background. This observation was also done in the full frame window mode with a medium filter and a total exposure time of 89 ks. The events are selected using the same method as for Abell 1650, and the effective exposure time of the LH is 42.8 ks for pn, 47.2 ks for MOS1 and 47.3 ks for MOS2. We estimate the difference of the particle background between Abell 1650 and LH from the total count rate in the region  $\theta \geq 10'$  (contamination due to cluster can be ignored) in the high energy band (10–12 keV for MOS and 12–14 keV for pn), as described in Pointecouteau et al. (2004). We find that the particle background level of Abell 1650 is about  $\alpha = 1.5$  times of that of LH. The outmost ring ( $13' - 16'$ ) was assumed to contain only these two kinds of background with no cluster contribution (we will discuss the rationality of this assumption in Sect. 4.1), and performed the same subtraction procedure as in Arnaud et al. (2002) to correct for these two background components.

The pn data have another source of contamination called out-of-time (OOT) events counted during the read-out (see Strüder et al. 2001). This contamination was also corrected in our analysis.

## 2.2 Spectral Deprojection

Abell 1650 appears to be a relaxed cluster of galaxies, therefore we assume its temperature structure to be spherically symmetric. Then, we divide this cluster into  $N = 8$  annular regions centered at the emission peak for the extraction of spectra (see Fig. 1). The minimum width of the rings was set at  $1'$ , wide enough for us to ignore the PSF effect of *XMM-Newton* EPIC, whose Full Width at Half Maximum (FWHM) is  $5''$  for MOS and  $6''$  for pn.

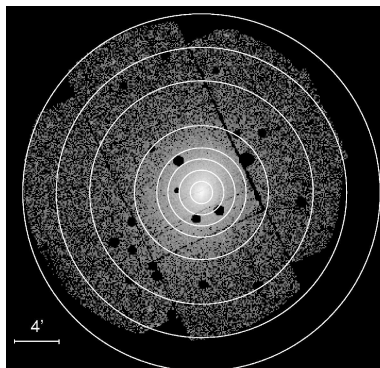


**Fig. 1** MOS1 image of Abell 1650 in sky coordinates excluding obvious point sources. The cluster was divided into eight annular regions centered at the emission peak for the extraction of spectra.

The deprojected spectra were calculated by subtracting the contribution from the outer regions for all spectral components, assuming the spectrum per unit volume within a given annulus to be the same. The deprojected spectrum of the  $i$ th shell is then calculated by subtracting the contributions from  $i+1$ th to the outmost shell from the annular spectrum of the corresponding radius (e.g., Matsushita et al. 2002; Nulsen & Böhringer 1995). We have assumed that there is no cluster emission in the outmost ring ( $13' - 16'$ ), so it can be subtracted as the background components directly as was done in Arnaud et al. (2002).

In our deprojection calculations, the effects of the point source regions (that were excluded) on the area of each region and the volume of each shell have been taken into account. For the two outmost rings, pixels with no exposure were also excluded. To each annular region an Ancillary Response File (ARF) was generated with the task *arfgen* and through which the vignetting correction (Arnaud et al. 2001) was administered.

Our calculations consist of the following steps:

$$ctrs(i, j) = \frac{cts(i, j)}{expo \cdot carf(i, j)} - \left( \frac{cts(N, j)}{expo} - \alpha \frac{ctb(N, j)}{expob \cdot backs(N)} \right) \cdot \frac{A(i)}{A(N)} \cdot \frac{1}{carf(N, j)}, \quad (1)$$

$$ctrb(i, j) = \frac{ctb(i, j)}{expob \cdot carf(i, j)} \cdot \frac{1}{backs(i)}, \quad (2)$$

where  $i$  is the number of the rings from  $N = 1$  to 8 and  $j$  is the energy channel from 1 to 4096 for pn and from 1 to 800 for MOS;  $cts(i, j)$  is the photon counts in the  $i$ th shell and the  $j$ th energy channel for Abell 1650 (including the backgrounds) and  $ctb(i, j)$  for LH;  $expo$  is the exposure time of Abell 1650 and  $expob$  for LH;  $\alpha$  is the particle background level of Abell 1650 compared to LH;  $backs(i)$  is the ratio of the area in the  $i$ th ring of LH to that of Abell 1650;  $A(i)$  is the area of Abell 1650 in the  $i$ th ring from which the area of the excluded point sources has been subtracted;  $carf(i, j)$  is the ratio of the effective area in the  $i$ th region to that in the central region in the  $j$ th energy channel, and  $carf(i, j)$  was used to correct for the vignetting; hence  $ctrs(i, j)$  is the count rate of Abell 1650 in the  $i$ th ring and the  $j$ th energy channel after the vignetting correction and the outmost residual background correction, and  $ctrb(i, j)$  is the count rate of LH after vignetting correction and transforming its area to that of Abell 1650.

Then, we begin the deprojection analysis

$$dcrs(i, j) = [ctrs(i, j) - \alpha \cdot ctrb(i, j) - \sum_{k=i+1}^N C_v(k, i) \cdot dcrcs(k, j)] / C_v(i, i), \quad (3)$$

where  $C_v(k, i)$  is the fraction of the volume of the  $k$ th shell projected to the  $i$ th ring;  $\sum_{k=i+1}^N C_v(k, i) \cdot dcrcs(k, j)$  is the sum of the projected count rate of the shells outside the  $i$ th; and  $dcrcs(i, j)$  is the deprojected count rate of Abell 1650 in the  $i$ th shell and the  $j$ th energy channel. Then, we write these data  $dcrcs(i, j)$  into the spectra which are the deprojected spectra.

### 3 SPECTRAL ANALYSIS

#### 3.1 Radial Deprojected Temperature Profile

The spectral analysis was carried out using XSPEC version 11.2.0 (Arnaud 1996). To check the temperature distribution, we fit the spectra of pn and MOS separately with the absorbed Mekal model:

$$\text{Model}_1 = \text{Wabs}(N_H) \times \text{Mekal}(T, z, A, norm), \quad (4)$$

where Wabs is a photoelectric absorption model (Morrison & McCammon 1983) and Mekal is a single-temperature plasma emission model (Mewe et al. 1985, 1986; Kaastra 1992; Liedahl et al. 1995), and the temperature  $T$ , metallicity  $A$  and normalization (emission measure) ‘*norm*’ are free parameters. We fix the absorption  $N_H$  to the Galactic value of  $1.54 \times 10^{20} \text{ cm}^{-2}$  (Dickey & Lockman 1990). The centroid energies of the Fe-K $\alpha$  lines in all the spectra were systematically larger than the value estimated from the optical redshift (Struble & Rood 1999), so we floated  $z$  of

**Table 1** The best-fit free parameters of Abell 1650 with a single-temperature model. The errors represent a confidence level of 90%.

Annulus $r$	$T^a$ (keV) ( $\chi_{\text{red}}^2/\text{dof}$ , $P^b$ )			$A^c$ (solar)	$norm^d$ ( $10^{-3}\text{cm}^{-5}$ )		$L_X^e$	$L_{\text{bol}}^f$
	MOS	pn	MOS+pn	MOS+pn	pn	MOS	( $10^{44}$ erg $\text{s}^{-1}$ )	
$0' - 1'$	$5.45 \pm 0.19$ (0.95/394, 0.74)	$4.97 \pm 0.15$ (1.16/376, 0.017)	$5.15 \pm 0.12$ (1.07/772, 0.10)	$0.48 \pm 0.04$	$4.36 \pm 0.06$	$4.68 \pm 0.07$	$1.17 \pm 0.02$	$2.52 \pm 0.03$
$1' - 2'$	$5.70 \pm 0.25$ (0.95/417, 0.785)	$5.17 \pm 0.25$ (1.22/397, 0.002)	$5.41 \pm 0.17$ (1.08/816, 0.05)	$0.34 \pm 0.05$	$5.13 \pm 0.10$	$5.45 \pm 0.10$	$1.33 \pm 0.03$	$2.90 \pm 0.05$
$2' - 3'$	$5.82^{+0.50}_{-0.38}$ (0.94/388, 0.789)	$5.29 \pm 0.33$ (1.20/334, 0.01)	$5.52 \pm 0.25$ (1.06/724, 0.118)	$0.26 \pm 0.07$	$4.71 \pm 0.11$	$4.82 \pm 0.11$	$1.18 \pm 0.03$	$2.58 \pm 0.06$
$3' - 4'$	$5.28 \pm 0.43$ (1.11/320, 0.08)	$4.73^{+0.40}_{-0.31}$ (1.18/288, 0.017)	$4.99 \pm 0.29$ (1.15/610, 0.01)	$0.29 \pm 0.08$	$3.83 \pm 0.12$	$4.16 \pm 0.13$	$1.00 \pm 0.03$	$2.09 \pm 0.06$
$4' - 6'$	$5.14^{+0.54}_{-0.51}$ (1.15/341, 0.03)	$3.95 \pm 0.32$ (1.16/299, 0.03)	$4.38 \pm 0.25$ (1.17/642, 0.002)	$0.11 \pm 0.08$	$4.52 \pm 0.14$	$4.22 \pm 0.13$	$1.06 \pm 0.03$	$2.04 \pm 0.06$
$6' - 10'$	$6.50^{+1.73}_{-1.18}$ (1.22/181, 0.02)	$3.89^{+0.66}_{-0.59}$ (1.25/147, 0.02)	$4.88^{+0.73}_{-0.61}$ (1.27/328, 0.001)	$0.15^{+0.22}_{-0.15}$	$3.80 \pm 0.24$	$3.62 \pm 0.25$	$0.91 \pm 0.06$	$1.84 \pm 0.12$
$10' - 13'$			$1.66^{+2.85}_{-0.77}$ (1.41/54, 0.03)	$0^{+0.16}_{-0.0}$	$2.30^{+1.13}_{-0.65}$	$2.20^{+1.35}_{-0.76}$	$0.49 \pm 0.21$	$0.65 \pm 0.28$

<sup>a</sup> Temperature in units of keV;<sup>b</sup> The null hypothesis probability of a spectra fitted in XSPEC;<sup>c</sup> Abundance in units of solar abundance derived from the ‘angr’ standard (Anders & Grevesse 1989) in XSPEC;<sup>d</sup> The normalized constant in units of  $10^{-3}\text{cm}^{-5}$ .  $norm = 10^{-14}/(4\pi(D(1+z))^2) \int n_e n_H dV$ , where  $D$  is the angular size distance to the source in cm and  $n_e$  is the electron density ( $\text{cm}^{-3}$ );<sup>e</sup> Luminosity in the energy range 0.1–2.4 keV in units of  $10^{44}$  erg  $\text{s}^{-1}$ ;<sup>f</sup> Bolometric luminosity (0.001–60.0 keV) in units of  $10^{44}$  erg  $\text{s}^{-1}$ .

the inner three spectra and fixed  $z = 0.0845$  for the outer spectra, and we found  $z = 0.0800^{+0.0003}_{-0.0012}$  from the inner spectra fitting. The spectra of the outer regions ( $r > 3'$ ) had lower signal-to-noise ratios compared with the inner spectra, so to the outer regions we excluded the energy bins around the strong instrumental fluorescence lines of Ni, Cu, and Zn in the energy range 7.8–9.0 keV from the pn spectral fitting and the fluorescence line of Al-K $\alpha$  in the energy range of 1.35–1.6 keV from the fitting of both pn and MOS spectra as was done in Takahashi & Yamashita (2003). The fitting results are listed in Table 1, where  $P$  is the null hypothesis probability of a spectrum fitted in XSPEC. We say we have a fit when  $P \geq 0.1$ , and when  $0.01 \leq P < 0.1$ , we say the fit is marginally acceptable. The spectrum of the central region ( $r < 1'$ ) for the pn data fitted by this single temperature model is shown in Figure 3a.

In order to derive the temperature profile of Abell 1650, we carried out a joint fit to the spectra of pn and MOS with this single temperature model with different normalizations. The fitting results are also listed in Table 1. The deprojected temperature profile was found to have a slight drop in the core (see the upper panel in Fig. 2) which may be connected with the gas cooling or/and the presence of ISM associated with the cD galaxy (Makishima et al. 2001), and beyond about  $3'$  the temperature tends to decrease. Then, we fit the temperature profile with a broken line, fitting the inner and outer parts separately with

$$T(r) = ar + b. \quad (5)$$

The best fit parameters are: for the inner part,  $a = 0.0038 \pm 0.0024 \text{ keV arcsec}^{-1}$ ,  $b = 4.98 \pm 0.21 \text{ keV}$ ; for the outer part,  $a = -0.0045 \pm 0.0016 \text{ keV arcsec}^{-1}$ ,  $b = 6.02 \pm 0.43 \text{ keV}$ ,  $\chi_{\text{red}}^2 = 0.84$ . The best-fit profile is shown as the solid broken line in the upper panel of Figure 2. The signal-to-noise ratio of the seventh ring is low. If we do not consider the seventh ring, the best-fit profile does not show much difference (the dotted line). So our following calculations of, e.g. mass and electron density, are all based on the solid profile. The diamonds in the bottom panel of Figure 2 are the deprojected abundance profile of Abell 1650. It can be seen that the abundance increases towards the cluster center, which indicates that the excess metal in the cluster center is produced in the cD galaxy and ejected into ICM (Makishima et al. 2001).

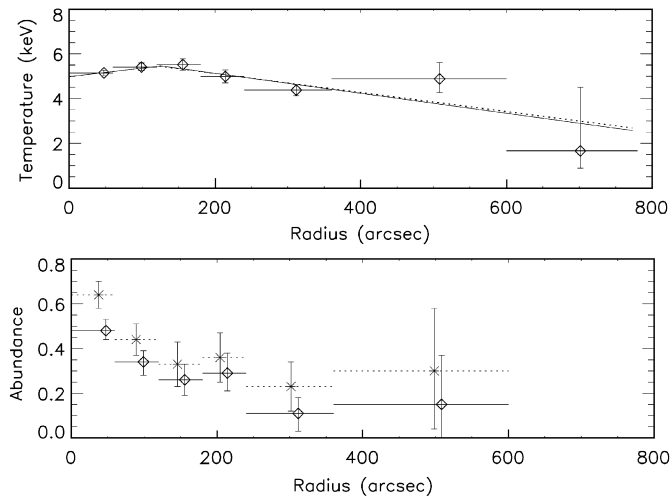


**Fig. 2** Deprojected radial temperature profile of Abell 1650, the solid broken line is the best-fit profile for all the rings and the dotted line for the rings 3–6. Bottom panel: deprojected radial abundance profile of Abell 1650. Diamonds: default solar abundance standard in XSPEC ‘angr’ (Anders & Grevesse 1989); stars: the widely used ‘grsa’ profile (Grevesse & Sauval 1998). We have offset the stars by  $10''$  to the left for better visibility. Error bars mark the 90% confidence level.

Our results do not differ much from those of Takahashi & Yamashita (2003) based on the same data, although what they have obtained are the projected temperature and abundance. Our deprojected results reveal the real properties of the gas in cluster directly, however, and make our following calculations, such as for the electron density and mass, more realistic.

Nevertheless, the solar abundance standard we used here is the XSPEC default one, ‘angr’ (Anders & Grevesse 1989), which has been known to be incorrect (McWilliam 1997; Grevesse & Sauval 1998). So we selected the most widely used one, ‘grsa’ (Grevesse & Sauval 1998) to fit the spectra. We found that the abundances became larger (see the stars in bottom panel of Fig. 2), while the temperatures changed little and are still within the error bars of the old result. Therefore, in our following calculations, such as the mass calculation, we still use the old temperature profile. We should also note that the new abundance standard did not give a better fitting than before.

### 3.2 Two-temperature Model

The temperature drop in the cluster center indicates that there exists a low temperature component, and for many clusters cool gas components were found in their centers, e.g., Abell 1835, Abell 1795 and M87 (Molendi & Pizzolato 2001). Since the MOS spectra can be fitted well by a single-temperature model, we fit the spectra of pn and the combined spectra of pn and MOS in the two central rings using a two-temperature model to study the properties of the central gas in Abell 1650:

$$\text{Model}_2 = \text{Wabs}(N_{\text{H}}) \times [\text{Mekal}(T_1, z, A_1, \text{norm}_1) + \text{Mekal}(T_2, z, A_2, \text{norm}_2)], \quad (6)$$

where the models and parameters have the same meanings as in Model<sub>1</sub>, and Model<sub>2</sub> means that two temperature components coexist in the central region. The fits now become much better and the results are given in Table 2, where  $f_{\text{vol}}$  is the volume filling fraction of the cool component. We find that the values of  $f_{\text{vol}}$  are very small, only about a few percent for both pn and pn+MOS, so the cool gas is only a minor component.  $F$  is the result of the simple  $F$ -test (Bevington 1969) which indicates the confidence level of using the two-temperature model instead of the single-temperature model, and from  $F$  we see that the replacement is significant. Figure 3b presents the spectrum of pn in the central region ( $r < 1'$ ) fitted by this two-temperature model with the two components

**Table 2** Best-fit parameters of Abell 1650 with a two-temperature model for the inner two regions of pn spectra and pn+MOS spectra. The error bars represent a confidence level of 90%.

	$r$	$T$ (keV)		$A$ (solar)		$norm$ ( $10^{-3} \text{cm}^{-5}$ )		$f_{\text{vol}}^{\text{a}}$	$\chi_{\text{red}}^2/\text{dof}$	$P$	$F^{\text{b}}$
		$T_1$	$T_2$	$A_1$	$A_2$	$norm_1$	$norm_2$				
pn	$0' - 1'$	$1.72^{+1.85}_{-0.95}$	$5.73^{+1.46}_{-2.57}$	$0.07^{+0.17}_{-0.07}$	$0.55^{+0.37}_{-0.09}$	$0.81^{+1.72}_{-0.57}$	$3.74^{+0.50}_{-1.81}$	2%	1.13/373	0.04	0.98
	$1' - 2'$	$1.17^{+0.50}_{-0.32}$	$7.42^{+2.35}_{-0.72}$	$0.02^{+0.06}_{-0.01}$	$0.41^{+0.98}_{-0.11}$	$1.94^{+0.34}_{-0.25}$	$4.00^{+0.42}_{-0.60}$	1%	1.08/394	0.12	> 0.99
pn+MOS	$0' - 1'$	$2.23^{+1.93}_{-0.84}$	$6.27^{+1.91}_{-0.68}$	$0.12^{+0.20}_{-0.11}$	$0.63^{+0.68}_{-0.11}$	$1.07^{+2.20}_{-0.65}$	$3.58^{+0.56}_{-2.33}$	3%	1.03/768	0.27	> 0.99
	$1' - 2'$	$1.14^{+0.39}_{-0.22}$	$6.89^{+0.69}_{-0.73}$	$0.01^{+0.04}_{-0.01}$	$0.42^{+0.07}_{-0.08}$	$1.27^{+0.50}_{-0.45}$	$4.53^{+0.37}_{-0.33}$	1%	1.02/812	0.38	> 0.99

<sup>a</sup>  $f_{\text{vol}}$  is the volume fraction of the cool component;

<sup>b</sup>  $F$  is the confidence level of using the two-temperature model instead of the single-temperature model.

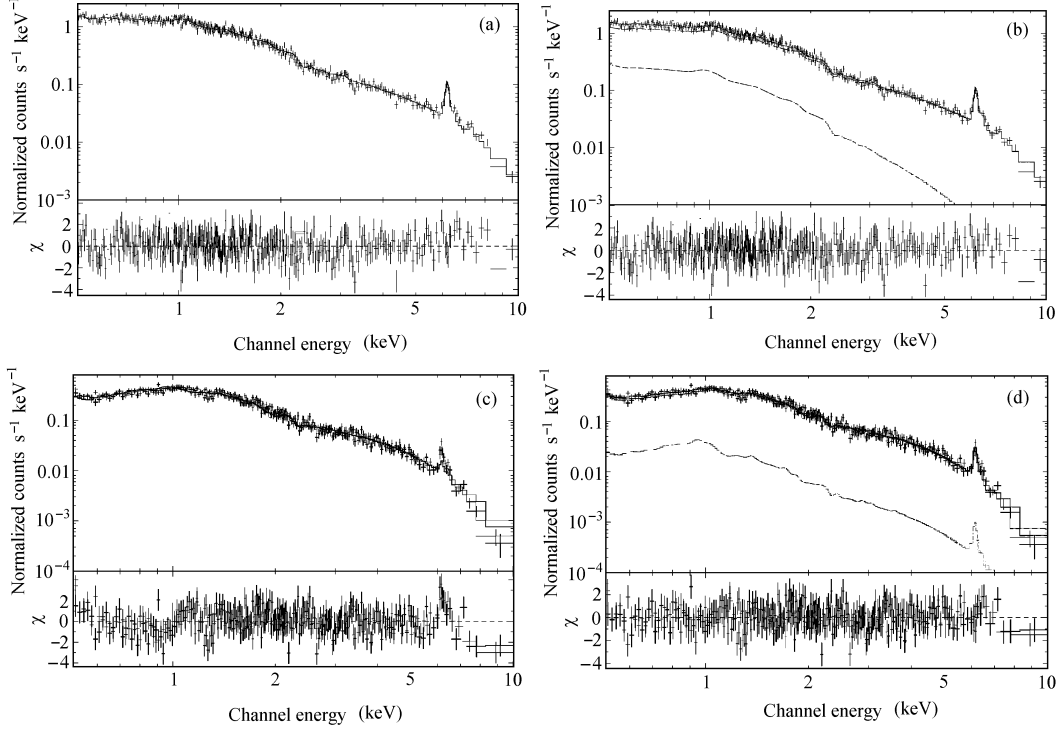


**Fig. 3** Spectra of the central region ( $r < 1'$ ) for the pn data ((a) and (b)) and the MOS data ((c) and (d)). MOS1: faint crosses; MOS2: bold crosses) of Abell 1650. (a) Fit by the single-temperature model. (b) Fit by the two-temperature model: the low temperature component is the curve below the crosses, which can be seen to be a minor component, contributing only a little to the emission. (c) Fit by the standard cooling flow model: there are large residuals in the soft and hard energy ends, making this model unacceptable. (d) Fit by a cooling flow model with an isothermal Mekal component. The isothermal and cooling flow components are plotted. The lower line represents the multiphase one which only contributes a little to the emission.

plotted, and we find that the cool gas only contributes a little to the emission. Therefore, we can infer that in the cluster center there may exist two gas components with different temperatures, but the cool component (1–2 keV) only accounts for a very small volume fraction.

From the fitting results above, we can estimate a normalization-weighted temperature of  $t_{\text{mean}} = 5.08 \pm 0.28$  keV from the single-temperature model. Since there exist two temperature

components in the cluster center, we find that the mean temperature of the hot gas is  $t_{\text{meanh}} = 5.50 \pm 0.55$ . This is in good agreement with the result ( $\sim 5.68^{+0.30}_{-0.27}$  keV) derived by Ikebe et al. (2002) from ASCA and ROSAT using a two-temperature model, and is lower than that of Markevitch et al. (1998) of  $\sim 6.70 \pm 0.80$  keV. We also obtained a luminosity (see Table 1),  $L_X$  (0.1–2.4 keV) =  $7.14 \pm 0.23 \times 10^{44}$  erg s $^{-1}$  and  $L_{\text{bol}}$ (0.001–60 keV) =  $14.62 \pm 0.33 \times 10^{44}$  erg s $^{-1}$ . The  $L_X$  calculated by Ikebe et al. (2002), when converted to our cosmology model, is  $7.33 \pm 0.79 \times 10^{44}$  erg s $^{-1}$ , which is consistent with our result. Reiprich & Böhringer (2002) have analysed the ROSAT data of Abell 1650 based on the temperature derived by Markevitch et al. (1998) from ASCA data and found that  $L_X = 7.308 \times 10^{44}$  erg s $^{-1}$  and  $L_{\text{bol}} = 17.955 \times 10^{44}$  erg s $^{-1}$ . Thus, our  $L_X$  value is consistent with what Reiprich & Böhringer (2002) derived, but our  $L_{\text{bol}}$  is much lower. This may be due to the difference of temperatures.

### 3.3 Absorbing Column Density

To investigate whether the observed  $N_{\text{H}}$  (derived from our fit) is consistent with the Galactic column density, we made fits with the parameter  $N_{\text{H}}$  left free. For many clusters, the best-fit column density derived from the MOS data is always in good agreement with the Galactic value, while that estimated from the pn data is always systematically smaller (Molendi & Pizzolato 2001), so we only use the MOS spectra here. For the lower signal-to-noise ratio of the outer regions, we only consider a joint fit to the inner four regions. The resulting column density  $N_{\text{H}}$  is  $1.25^{+0.56}_{-0.53} \times 10^{20}$  cm $^{-2}$  for the MOS1 spectra and  $0.93^{+0.98}_{-0.93} \times 10^{20}$  cm $^{-2}$  for the MOS2 spectra, both consist with the Galactic value  $\sim 1.54 \times 10^{20}$  cm $^{-2}$  within the error bars. Therefore, the spectral fits with the Galactic column density value are reliable.

### 3.4 Mass Deposition Rate

The slight temperature drop in the central part of Abell 1650 perhaps means that there exists a cooling flow in its center. In the following we estimate the parameters of the cooling flow.

First, we estimate the cooling time in Abell 1650,  $t_{\text{cool}}$  — the time scale that the hot gas loses all its thermal energy. The thermal energy in shell  $i$  is

$$t_{\text{cool}}(i) = \frac{5 N(i) k_B T(i)}{2 L_{\text{bol}}(i)}, \quad (7)$$

where  $k_B$  is the Boltzmann constant,  $L_{\text{bol}}(i)$  the bolometric luminosity (see Table 1) and  $N(i)$  the particle number density of the  $i$ th shell. Since

$$\text{norm}(i) = 10^{-14} / (4\pi(D(1+z))^2) \cdot \int n_e n_{\text{H}} dV, \quad (8)$$

where  $\text{norm}(i)$  is the normalized constant of the  $i$ th ring listed in Table 1 and  $D$  is the angular size distance to the source in cm, we can derive the deprojected electron density  $n_e(i)$  of each shell. Thus the particle number density  $N(i)$  can be calculated by

$$N(i) = \frac{1.17 \times n_e(i)}{\mu}, \quad (9)$$

where  $\mu$  is the mean molecular weight of the gas in units of  $m_p$ , and the proton mass, for a fully ionized gas with the standard cosmic abundance of the elements, a suitable value is  $\mu = 0.6$ . Therefore, the cooling time in each shell can be estimated, and  $t_{\text{cool}}$  of the inner two regions are given in Table 3. The cooling flow radius is the radius at which the hot gas loses all its thermal energy within a specified cooling time scale, usually the age of the universe of about  $1.3 \times 10^{10}$  yr. So it can be estimated that the cooling flow radius is:  $r_{\text{cool}} = 144.2 \pm 2.5$  kpc.

Then we used the MOS data, thought to be better for the determination of  $N_{\text{H}}$  and hence the mass deposition rate (Molendi & Pizzolato 2001), to calculate the mass deposition rate of Abell 1650 by the spectral method, i.e. to fit the deprojected spectra in XSPEC by the cooling flow

**Table 3** Cooling time scale and cooling flow rate in the the inner two rings of Abell 1650. The error bars refer to 68% confidence level.  $1' = 127.9$  kpc.

$r$	$t_{\text{cool}}$ (yr)	$\dot{M}$ ( $M_{\odot} \text{ yr}^{-1}$ )
$0' - 1'$	$9.75 \pm 0.16 \times 10^9$	$158.6 \pm 2.6$
$1' - 2'$	$2.55 \pm 0.06 \times 10^{10}$	$250.5 \pm 5.9$

**Table 4** The best-fit parameters for the central two rings of the MOS data by the cooling flow model with the low  $T$  fixed at 0.01 keV and free respectively. The errors refer to the 90% confidence level.  $1' = 127.9$  kpc.

$r$	low $T_{cf}$ (keV)	high $T_{cf}$ (keV)	$A$ (solar)	$\dot{M}^a$ ( $M_{\odot} \text{ yr}^{-1}$ )	$\Delta N_{\text{H}}^b$ ( $10^{22} \text{ cm}^{-2}$ )	$\chi^2_{\text{red}}/\text{dof}$	$P$
$0' - 1'$	$3.3^{+2.0}_{-0.8}$	$8.4^{+2.1}_{-2.8}$	$0.53^{+0.08}_{-0.07}$	$234.6^{+210740}_{-81.2}$	$0.0^{+0.003}_{-0.0}$	0.95/392	0.731
	0.01 (fix)	$17.4^{+0.7}_{-1.1}$	$0.25^{+0.05}_{-0.07}$	$80.2^{+4.4}_{-2.6}$	$0.035^{+0.008}_{-0.007}$	1.23/393	0.001
$1' - 2'$	$4.3^{+1.3}_{-1.8}$	$7.5^{+4.1}_{-1.6}$	$0.39 \pm 0.09$	$425.5^{+7.1 \times 10^7}_{-269.0}$	$0.0^{+0.005}_{-0.0}$	0.95/415	0.764
	0.01 (fix)	$17.3^{+2.0}_{-2.1}$	$0.03^{+0.10}_{-0.03}$	$91.2^{+10.4}_{-7.4}$	$0.02^{+0.02}_{-0.01}$	1.06/416	0.206

<sup>a</sup>  $\dot{M}$  is the mass deposition rate; <sup>b</sup>  $\Delta N_{\text{H}}$  is the intrinsic absorption.

**Table 5** The same as Table 4 but for the cooling flow model with an isothermal component: Mekal+Mkcf flow.

$r$	$T_{\text{mekal}}$ (keV)	low $T_{cf}$ (keV)	high $T_{cf}$ (keV)	$A$ (solar)	$norm$ ( $10^{-3} \text{ cm}^{-5}$ )	$\dot{M}$ ( $M_{\odot} \text{ yr}^{-1}$ )	$\Delta N_{\text{H}}$ ( $10^{22} \text{ cm}^{-2}$ )	$\chi^2_{\text{red}}/\text{dof}$	$P$
$0' - 1'$	$5.77^{+0.44}_{-0.30}$	0.01 (fix)	$=T_{\text{mekal}}$	$0.54 \pm 0.08$	$4.33^{+0.24}_{-0.30}$	$10.2^{+11.5}_{-7.5}$	$0.0^{+0.11}_{-0.0}$	0.95/392	0.775
$1' - 2'$	$5.74^{+0.54}_{-0.29}$	0.01 (fix)	$=T_{\text{mekal}}$	$0.39 \pm 0.09$	$5.32^{+0.18}_{-0.38}$	$1.6^{+12}_{-1.6}$	0.0 (fix)	0.95/416	0.775

model. Since the contribution of the ambient gas has been excluded by the deprojection, we select the standard cooling flow model:

$$\text{Model}_3 = \text{Wabs}(N_{\text{H}}) \times [\text{Zwabs}(\Delta N_{\text{H}}) \times \text{Mkcf flow}(\dot{M})], \quad (10)$$

where  $\text{Wabs}$  has been described in Section 3.1.  $\text{Zwabs}$  is an intrinsic photoelectric absorption model (Morrison & McCammon 1983), and  $\text{Mkcf flow}$  a cooling flow model (Fabian 1988);  $\Delta N_{\text{H}}$  is the intrinsic absorption and  $\dot{M}$  the rate of gas cooling out of the flow. We fit the spectra of MOS1 and MOS2 simultaneously with this model, and the fitting results of the central two regions are listed in Table 4. Now, Peterson et al. (2001) found that Abell 1835 required a cut-off temperature  $\sim 2.7$  keV when fitting with a cooling flow model. We followed this lead and found that a cut-off temperature, low  $T \sim 3 - 4$  keV, is needed to fit the spectra satisfactorily. If we fix low  $T = 0.01$  keV as required by the standard cooling flow model, then the  $\chi^2$  value of the central region is much higher, giving an unacceptable value of  $P$  (see Fig. 3c), and for the second ring the temperature high  $T = 17.3^{+2.0}_{-2.1}$  is unreasonably high. Thus, the standard cooling flow model cannot fit the spectra satisfactorily.

Adding an isothermal Mekal component, the cooling flow model becomes

$$\text{Model}_4 = \text{Wabs}(N_{\text{H}}) \times [\text{Mekal}(T, z, A, norm) + \text{Zwabs}(\Delta N_{\text{H}}) \times \text{Mkcf flow}(\dot{M})]. \quad (11)$$

With this model, the fits are much better, see Figure 3d and Table 5. We find that the mass deposition rate in the region  $r < 1'$  is  $10.2^{+11.5}_{-7.5} M_{\odot} \text{ yr}^{-1}$  and  $1.6^{+12}_{-1.6} M_{\odot} \text{ yr}^{-1}$  within  $1' < r < 2'$ . Or, at the cooling flow radius  $r_{\text{cool}} = 144.2$  kpc, the mass deposition rate is  $10.4^{+11.6}_{-7.5} M_{\odot} \text{ yr}^{-1}$ .

Another method to calculate the mass deposition rate is the spatial method. Based on the energy conservation, this method can be expressed by (White, Jones & Forman 1997)

$$L_{\text{bol}}(i) = \dot{M}(i)[h(i) + f(i) \Delta \phi(i)] + \sum_{i'=1}^{i'-i-1} \dot{M}(i')[\Delta h(i) + \Delta \phi(i)], \quad (12)$$

where  $L_{\text{bol}}(i)$  is the bolometric luminosity in the  $i$ th shell (as shown in Table 1),  $\dot{M}(i)$  the mass deposition in shell  $i$ ,  $\sum_{i'=1}^{i'-i-1} \dot{M}(i')$  the mass of gas that needs to pass through shell  $i$  to give rise to the radiation and mass deposition in interior shells,  $\Delta \phi(i)$  the change in the gravitational potential,  $h(i) = \frac{5}{2}kT(i)/\mu m_p$ ,  $f(i)$  a fraction of the overall change in the cluster potential, and in this analysis  $f(i) = 1$  is used. The first two terms in this equation represent the mass drops out of shell  $i$ , and the second two terms represent the mass that flows through to the next interior shell. Using this method we calculate the mass deposition rates of the inner two regions (also see Table 3). Within the cooling flow radius  $\sim 144.2$  kpc, the mass deposition rate is about  $190.5 \pm 3.4 M_{\odot} \text{ yr}^{-1}$ .

White et al. (1997) have analysed the *Einstein Observatory* imaging data of Abell 1650 using this spatial method and found that the mass deposition rate is  $122^{+168}_{-122} M_{\odot} \text{ yr}^{-1}$  and the cooling flow radius is  $110^{+119}_{-110}$  kpc, while the results derived by Peres et al. (1998) using the ROSAT data are  $\dot{M} = 280^{+464}_{-89} M_{\odot} \text{ yr}^{-1}$  and  $r_{\text{cool}} = 165^{+103}_{-24}$  kpc. Both results are marginally consistent with our spatial results.

The mass deposition rate derived from the spatial method gives the total loss rate of the energy in absence of any heating process, which is much larger than that from the spectral method containing the mass deposition rate only during the cooling flow. The discrepancy between these two methods has been found and discussed in Etti et al. (2002) for Abell 1795, which implied that some heating processes that can substantially reduce the mass deposition have to be reconsidered, such as the energy feedback of the central AGN (e.g., M87, Matsushita et al. 2002; Böhringer et al. 2002).

## 4 MASS DETERMINATION

### 4.1 Deprojected Electron Density

We divided the cluster into 17 annular regions centered on the emission peak out to  $13'$ , the width of each annulus being so chosen that the total count in the region exceed 20000. The deprojected count rate in each corresponding shell,  $Ctr(i)$ , was calculated by the deprojection technique. Since the temperature and abundance profiles are known, we can simulate the spectrum of each shell from  $T(i)$ ,  $A(i)$  and  $Ctr(i)$  in XSPEC. Then fitting the simulated spectra with Model<sub>1</sub>, the normalizing constant  $norm(i)$  and its error in each shell are determined, and the error in the outermost region ( $10' - 13'$ ) is about 10%. Then we can derive the deprojected electron density  $n_e$  of each region from Equation (8), see the stars in Figure 4.

We fit the electron density with the following double- $\beta$  model appropriate for electron density, rather than the usual double- $\beta$  model used to fit the surface brightness (see Chen et al. 2003):

$$n_e(r) = n_{01} \left[ 1 + \left( \frac{r}{r_{c1}} \right)^2 \right]^{-\frac{3}{2}\beta_1} + n_{02} \left[ 1 + \left( \frac{r}{r_{c2}} \right)^2 \right]^{-\frac{3}{2}\beta_2}. \quad (13)$$

The best-fit parameters are:  $n_{01} = 0.00134 \pm 0.00015 \text{ cm}^{-3}$ ,  $r_{c1} = 6.34 \pm 1.13 \text{ arcmin}$ ,  $\beta_1 = 2.41 \pm 0.63$ ,  $n_{02} = 0.0187 \pm 0.0005 \text{ cm}^{-3}$ ,  $r_{c2} = 0.501 \pm 0.012 \text{ arcmin}$ ,  $\beta_2 = 0.406 \pm 0.019$ ,  $\chi^2_{\text{red}} = 3.4$ , and  $\text{dof} = 11$ . The best-fit profile is shown by the solid line in Figure 4.

Extrapolating the electron density profile  $n_e(r)$  outwards, we estimate that the signal-to-noise ratio in the outmost ring ( $13' - 16'$ ) is very low ( $< 10\%$ ), so its projected effect to the inner rings can be ignored, that is, it is reasonable to assume that there is no cluster emission in the outmost ring.

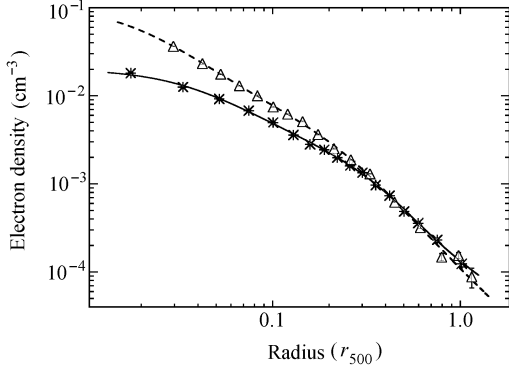


**Fig. 4** Electron density profile of Abell 1650 (stars) and Abell 1835 (triangles). The error bars are at the 68% confidence level. The solid line is the best-fit profile of Abell 1650 with a double- $\beta$  model, and the dashed line, for Abell 1835.

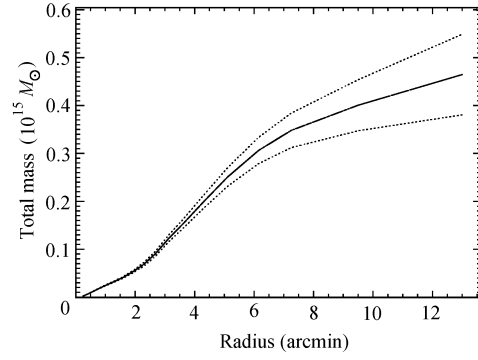


**Fig. 5** Total mass profile of Abell 1650. The error bars (dotted lines) are at the 68% confidence level.

## 4.2 Total Mass

Once we have obtained the deprojected radial profiles of electron density  $n_e(r)$  and temperature  $T(r)$  of Abell 1650, together with the assumptions of hydrostatic equilibrium and spherical symmetry, the integrated total mass of the cluster within radius  $r$  can be calculated with the following equation (Fabricant et al. 1980):

$$M_{\text{tot}}(< r) = -\frac{k_B T r^2}{G \mu m_p} \left[ \frac{d(\ln n_e)}{dr} + \frac{d(\ln T)}{dr} \right], \quad (14)$$

where  $k_B$  is the Boltzmann constant,  $G$  the gravitational constant,  $m_p$  the proton mass and  $\mu$  has the same meaning as in Equation (9). The total mass profile is shown in Figure 5, and  $M_{\text{tot}} = 4.65 \pm 0.84 \times 10^{14} M_\odot$  within  $13'$  at the 68% confidence level.

A physically meaningful radius for the mass measurement is defined as  $r_{500}$  which is the radius within which the mean gravitational mass density  $\langle \rho_{\text{tot}} \rangle = 500 \rho_c$ , where  $\rho_c = 3H^2/(8\pi G)$  is the critical cosmic matter density. For our calculations, we use the zero redshift value, i.e.  $\rho_c = 4.70 \times 10^{-30} \text{ g cm}^{-3}$ . Then we find that for Abell 1650  $r_{500} = 1.44 \pm 0.07 \text{ Mpc}$ , corresponding to  $11.3' \pm 0.6'$ , and the total mass within it is about  $M_{500} = 4.34 \pm 0.69 \times 10^{14} M_\odot$ .

Reiprich & Böhringer (2002) obtained  $r_{500} = 1.88_{-0.21}^{+0.28} \text{ Mpc}$  and  $M_{500} = 9.62_{-2.92}^{+4.91} \times 10^{14} M_\odot$  for Abell 1650 using the ROSAT data based on the temperature derived by Markevitch et al. (1998) from ASCA data, which are larger than our results. This might be due to the different temperatures used in the calculations.

## 5 COMPARISON WITH A LARGE COOLING FLOW CLUSTER (ABELL 1835) AND SOME OTHER CLUSTERS

From the analysis above, we know that Abell 1650 is a galaxy cluster with a small mass deposition rate  $\sim 10.4_{-7.5}^{+11.6} M_\odot \text{ yr}^{-1}$ . Here, we compare it with a large cooling flow cluster Abell 1835 ( $\dot{M} = 656_{-360}^{+403} M_\odot \text{ yr}^{-1}$  within  $0.75'$ , Jia et al. 2004) and some other clusters, so as to study if there exist any differences in the properties of small and large cooling flow clusters, and further, how the different cooling flows originated. For convenience in comparison, we scale the radial coordinate to  $r_{500}$ . For Abell 1835,  $r_{500} = 2.00 \pm 0.23 \text{ Mpc}$ , corresponding to  $6.7' \pm 0.44'$  and  $M_{500} = 1.16 \pm 0.16 \times 10^{15} M_\odot$ .

## 5.1 Temperature Profile

The temperature of Abell 1835 drops sharply at the center (see the triangles in Fig. 6), while that of Abell 1650 (stars) drops only slightly towards the center. Below we shall further discuss the temperature drop at the centre as a possible signature of cooling flow.

In Figure 6 we compare our two clusters' temperatures with the temperature profile derived by Allen et al. (2001) from a sample of six massive cooling flow clusters observed with *Chandra* (the dotted lines). In the figure, all the radii have been normalized by  $r_{2500}$ , within which the mean gravitational mass density is  $2500\rho_c$ , and the temperatures are in units of  $T_{2500}$ , the temperature at  $r_{2500}$ . For Abell 1650  $r_{2500} = 733 \pm 21$  kpc  $= 5.7' \pm 0.2'$  and for Abell 1835  $r_{2500} = 918 \pm 84$  kpc  $= 3.1' \pm 0.3'$ . It can be seen that the temperature of Abell 1835 is in good agreement with the universal temperature profile (Allen et al. 2001). While the temperature profile of Abell 1650 is not, in particular, its temperature does not show a sharp decrease at the center.

The solid line in Figure 6 presents a quasi-steady state temperature profile for the massive cooling flow clusters predicted by McCarthy et al. (2004), which is in good agreement with the temperature distribution of Abell 1835. Abell 1650 is a small cooling flow cluster which only has a slightly decreased temperature in its center, consistent with the simulative results of small or non-cooling flow cluster in McCarthy et al. (2004).

## 5.2 Gravitational Potential Well

The temperature in the very central region of a cluster has not been known clearly, so we select  $r = 0.02 r_{500}$  as the zero point of the clusters' gravitational potential well, defining the gravitational potential well  $V(r)$  at radius  $r$ , as:

$$V(r) = \int_{0.02r_{500}}^r \frac{GM(r)}{r^2} dr, \quad (15)$$

where  $G$  is the gravitational constant and  $M(r)$  is the total mass within  $r$  defined by Equation (14). The potential wells of Abell 1650 and Abell 1835 are plotted as the solid lines in Figure 7. We also plot the potential wells of the large cooling flow cluster PKS 0745–191,  $\dot{M} = 364_{-94}^{+97} M_{\odot} \text{ yr}^{-1}$  (Chen et al. 2003); the moderate cooling flow cluster Abell 1413,  $\dot{M} = 58.9 M_{\odot} \text{ yr}^{-1}$  (Pratt & Arnaud 2002); the small cooling flow clusters Abell 1991 (Pratt & Arnaud 2005) with  $\dot{M} \leq 25 M_{\odot} \text{ yr}^{-1}$  (Sharma et al. 2004) and Abell 1983 with  $\dot{M} = 6 M_{\odot} \text{ yr}^{-1}$  (Pratt & Arnaud 2003); and the non-cooling flow cluster Coma (Reiprich & Böhringer 2002).

It can be seen that a steeper potential well in the central region ( $r = 0.1 \sim 0.2 r_{500}$ ) corresponds to a large cooling flow (Abell 1835 and PKS 0745–191), and a flatter potential well corresponds to a small cooling flow (Abell 1650, Abell 1991 and Abell 1983). This can be explained by steeper potential well making it easy for outside matter to fall in and making it difficult for inside matter to escape. So the gas density in the center of cluster with steeper potential well will be higher, and the mass deposition rate larger and the temperature lower. Therefore, Abell 1835 exhibits a steeper potential well than does Abell 1650. It is worth noting that Coma is a massive cluster with  $M_{500} = 1.2 \pm 0.13 \times 10^{15} M_{\odot}$  (Reiprich & Böhringer 2002), a mass close to that of Abell 1835, but there is no cooling flow in its center. This may be due to its flatter potential well profile in the core.

The indications are that the shape of the gravitational potential well at the cluster center is an important property when discriminating different cluster types. The one with a steeper potential well has a larger cooling flow and that with a flatter potential well has a smaller cooling flow.

Makishima et al. (2001) have found that a cluster with a 'central excess emission' (CEE) in its center has a steeper potential well. Our result is similar to theirs, since a CEE cluster usually has a cooling flow in its center. *XMM-Newton* is the most sensitive telescope with high spatial and spectral resolution, and this makes its determination of potential well more reliable than before. Here, what we emphasized is that we can derive the relation of the cooling flow rate and the shape of the gravitational potential well in cluster center.

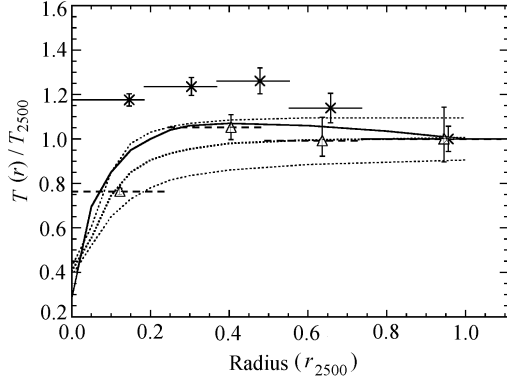


**Fig. 6** Temperature profile of Abell 1650 (stars and solid lines) and Abell 1835 (triangles and dashed lines) within  $r_{2500}$ , and comparison with the universal temperature profile (dotted lines) of Allen et al. (2001) derived from a sample of six massive, cooling flow clusters observed with *Chandra*. The bold solid line presents the predicted temperature profile of McCarthy et al. (2004) for relaxed massive, cooling flow clusters.

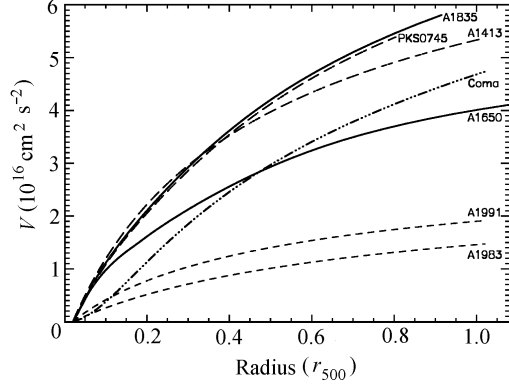


**Fig. 7** Profiles of the gravitational potential well for the large cooling flow clusters, i.e., Abell 1835 and PKS 0745–191 (Chen et al. 2003), the moderate cooling flow cluster Abell 1413 (Pratt & Arnaud 2002), the small cooling flow clusters Abell 1650, Abell 1991 (Pratt & Arnaud 2005), Abell 1983 (Pratt & Arnaud 2003), and the non-cooling flow cluster Coma (Reiprich & Böhringer 2002). These data are all from *XMM-Newton* except Coma which is from ASCA and ROSAT observations.

### 5.3 Electron Density

We also plot the electron density of Abell 1835 in Figure 4 fitted with a double- $\beta$  model (Eq. (13)) with the best-fit parameters:  $n_{01} = 0.0039 \pm 0.0009 \text{ cm}^{-3}$ ,  $r_{c1} = 1.56 \pm 0.33 \text{ arcmin}$ ,  $\beta_1 = 1.10 \pm 0.27$ ,  $n_{02} = 0.10 \pm 0.01 \text{ cm}^{-3}$ ,  $r_{c2} = 0.12 \pm 0.01 \text{ arcmin}$ ,  $\beta_2 = 0.60 \pm 0.04$ ,  $\chi_{\text{red}}^2 = 12.3$  and dof=11. It can be seen that the electron density of Abell 1835 in the central region is much higher than that of Abell 1650. This is consistent with the result derived in Section 5.2 that the gravitational potential well of Abell 1835 is much steeper and it is more difficult for the matter inside to escape. It is also interesting that when  $r > 0.2 r_{500}$  the two densities approach to almost the same value. We can infer that the differences in central concentration and central temperature gradients are the main identifications of these two types of clusters.

### 5.4 Gas Mass Fraction

In galaxy clusters, gas is an important component, which has a temperature of a few keV, roughly tracing the depth of the gravitational potential wells of the system.

From the electron density we can calculate the gas mass, and then the gas mass fraction defined as  $f_{\text{gas}}(r) = M_{\text{gas}}(r)/M_{\text{tot}}(r)$ . Figure 8 shows the gas mass fraction of Abell 1650 and Abell 1835:  $f_{\text{gas}}$  of Abell 1650 is significantly lower than that of Abell 1835 in the central region, and that of both clusters rise rapidly within  $0.2 r_{500}$ , but beyond which  $f_{\text{gas}}$  of Abell 1650 remains increasing while that of Abell 1835 keeps approximately constant at about  $f_{\text{gas}} = 0.25$ . This also can be explained as the result of the gravitational potential well described in Section 5.2, especially in regard of additional energy input, e.g., supernova-driven galactic wind, whose effect is smaller on massive clusters with steeper gravitational potential wells than on low mass clusters with flatter gravitational potential wells (e.g. Castillo-Morales & Schindler 2003). Then, according to the shape of the potential well presented in Figure 7, outflows in Abell 1835 will reach much farther out than those in Abell 1650. So a cluster with a flatter gravitational potential well tends to have a gas mass fraction increasing with radius.

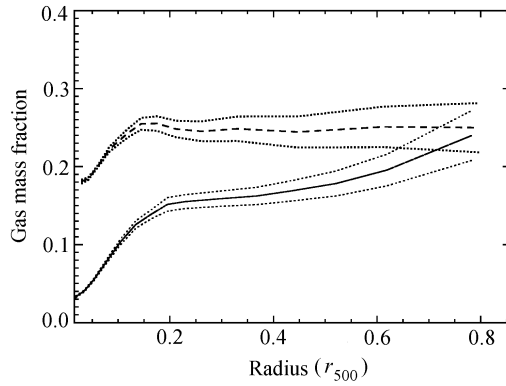


**Fig. 8** Gas mass fraction profile of Abell 1650 (solid line) and Abell 1835 (dashed line). The error bars (dotted lines) are at the 68% confidence level.

### 5.5 The Internal and Potential Energy

We assume that the baryons and the dark matter began to collapse together from a uniform state with the critical cosmological density  $\rho_c = 1.88h^2 \times 10^{-29} \text{ g cm}^{-3}$ , and have evolved now into a virialized cluster. According to energy conservation, the reduction of the potential energy of the gas in clusters should transform into its internal energy and radiation during the collapse, that is, ignoring the pre-heating and the energy possibly obtained from the dark matter during the collapse, for the gas in cluster the change in its gravitational potential energy should equal to the sum of its internal energy and its radiated energy.

Then, we calculate the potential energy  $E_V$ , internal energy  $E_T$  and radiated energy  $E_L$  of the gas in Abell 1650 and Abell 1835 respectively at the present time within  $r_{500}$ , assuming that the emitting time is equal to the age of the universe  $\sim 1.3 \times 10^{10}$  yr. The results are:  $E_V = -3.10 \pm 0.32 \times 10^{63}$  erg,  $E_T = 2.42 \pm 0.24 \times 10^{63}$  erg and  $E_L = 0.79 \pm 0.09 \times 10^{63}$  erg for Abell 1650;  $E_V = -1.37 \pm 0.22 \times 10^{64}$  erg,  $E_T = 1.16 \pm 0.17 \times 10^{64}$  erg and  $E_L = 0.49 \pm 0.09 \times 10^{64}$  erg for Abell 1835. This indicates that the energy of the gas in cluster is approximately conservative during the collapsing process.

### 5.6 Summary of the Comparison

Through a comparison of the properties of the small cooling flow cluster Abell 1650 with the large cooling flow cluster Abell 1835 and some other clusters, we found little difference in overall properties, such as  $f_{\text{gas}}$  of the whole cluster and the energy conservation of gas during collapse; however, we found that cooling has a significant effect on the clusters' properties in the center, e.g., temperature  $T$  and electron density  $n_e$ .

In addition, we found that, major mergers and entropy injection excepted, the shape of the gravitational potential well is a natural property to determine whether a cluster is a large, small or non-cooling flow cluster, and through which all the other properties can be explained. However, a wider exploration is needed to clarify which mechanism proposed here is the dominant factor for the different cooling flows in clusters. At the same time, a statistical analysis of the gravitational potential well shapes is useful, with larger cluster samples from the higher quality observations of *XMM-Newton* and *Chandra*.

## 6 CONCLUSIONS

We have presented a detailed analysis of an *XMM-Newton* observation of the galaxy cluster Abell 1650 with the deprojection technique applied. Through spectrum fitting we derived the deprojected temperature profile, which shows a slight drop in the core and a gradual decrease beyond  $3'$ ,

consistent with that found by Takahashi & Yamashita (2003). The abundance is higher in the cluster center, which may be caused by the cD galaxy (Makishima et al. 2001). The central two regions can be better fitted with a two-temperature model, and a cooler gas about  $1\sim 2$  keV was found in the cluster center which may be due to the gas cooling and/or the ISM associated with the cD galaxy (Makishima et al. 2001). Weighted by normalizations, we derived mean temperature,  $t_{\text{mean}} = 5.08 \pm 0.20$  keV from a single-temperature model and  $t_{\text{meanh}} = 5.50 \pm 0.55$  keV from the hot gas of a two-temperature model, which is in agreement with what derived from ASCA and ROSAT using a two-temperature model (Ikebe et al. 2002), but lower than that derived by Markevitch et al. (1998). We also obtained the luminosity of Abell 1650,  $L_X = 7.14 \pm 0.23 \times 10^{44}$  erg s $^{-1}$ , consistent with the results of Ikebe et al. (2002) and Reiprich & Böhringer (2002), but our  $L_{\text{bol}} = 14.62 \pm 0.33 \times 10^{44}$  erg s $^{-1}$  is much lower.

Then we calculated the cooling time scale of the inner two regions and obtained the cooling flow radius as  $144.2 \pm 2.5$  kpc. The standard cooling flow model can not fit the spectra satisfactorily. After adding an isothermal Mekal component, the fits become acceptable, and the mass deposition rate is about  $10.4^{+11.6}_{-7.5} M_{\odot} \text{ yr}^{-1}$  within the cooling flow radius. By another method – the spatial method,  $\dot{M} = 190.5 \pm 3.4 M_{\odot} \text{ yr}^{-1}$ , which is marginally consistent with the ROSAT result of  $280^{+464}_{-89} M_{\odot} \text{ yr}^{-1}$  derived using the same method (Peres et al. 1998). The discrepancy between these two methods implies that there exist some other energy sources that can heat the gas and prevent the gas from cooling.

From the isothermal model we derived the deprojected electron density profile  $n_e(r)$ , then together with the deprojected temperature profile  $T(r)$ , we obtained that  $r_{500} = 1.44 \pm 0.07$  Mpc and  $M_{500} = 4.34 \pm 0.69 \times 10^{14} M_{\odot}$ , which are lower than those derived by Reiprich & Böhringer (2002). This indicates that at least the properties of some clusters in the ASCA and ROSAT samples need to be modified and it is necessary to rebuild a new cluster sample of *XMM-Newton*, which may modify the previously obtained important relations of clusters, such as the  $L_X - T$  and  $M - T$  relations.

In addition, we compared the properties of Abell 1650 with those of Abell 1835 and some other clusters, and found that: (1) the temperature drop in the cluster center may be a signature for cooling flow; (2) a large cooling flow cluster has a steeper gravitational potential well in the central region which determines the electron density distribution and the relative gas extent, and this result is consistent with that of Makishima et al. (2001); (3) the type a particular cluster belongs to may be determined by the shape of the gravitational potential well, in addition to entropy injection and/or cluster merger; and (4) the energy of gas in both clusters is approximately conservative during the cluster forming process. From the comparison above we concluded that some overall properties of clusters, such as  $f_{\text{gas}}$  of the whole cluster and the energy conservation of gas, are not different for large and small cooling flow clusters while cooling has a significant effect on the properties ( $T$  and  $n_e$ ) in the cluster center.

**Acknowledgements** We would like to thank the referee for careful and helpful comments improving the paper significantly. We also thank F.J. Lu for useful discussions and suggestions. This research is partially supported by NSFC G10273010 and the State Basic Science Research of China (TG 20000776).

## References

- Abell G. O., Corwin H. G. Jr, Olowin R. P., 1989, ApJS, 70, 1  
 Allen S. W., Schmidt R. W., Fabian A. C., 2001, MNRAS, 328, 37  
 Anders E., Grevesse N., 1989, GeCoA, 53, 197  
 Arnaud K. A., 1996, Astronomical Data Analysis Software and Systems V, eds. Jacoby G. and Barnes J., p.17, ASP Conf. Series Vol. 101  
 Arnaud M., Majerowicz S., Lumb D., et al., 2002, A&A, 390, 27  
 Arnaud M., Neumann D. M., Aghanim N. et al., 2001, A&A, 365, L80  
 Bevington P. R., 1969, Data Reduction and Error Analysis for the Physical Sciences (New York: McGraw-Hill)

- Böhringer H., Matsushita K., Churazov E. et al., 2002, *A&A*, 382, 804  
Castillo-Morales A., Schindler S., 2003, *A&A*, 403, 433  
Chen Y., Ikebe Y., Böhringer H., 2003, *A&A*, 407, 41  
Dickey J. M., Lockman F. J., 1990, *ARA&A*, 28, 215  
Ettori S., Fabian A. C., Allen S. W. et al., 2002, *MNRAS*, 331, 635  
Fabian A. C., 1988, *Sci*, 242, 1586  
Fabricant D., Lecar M., Gorenstein P., 1980, *ApJ*, 241, 552  
Grevesse N., Sauval A. J., 1998, *SSRv*, 85, 161  
Ikebe Y., Reiprich T. H., Böhringer H. et al., 2002, *A&A*, 383, 773  
Jia S. M., Chen Y., Lu F. J. et al., 2004, *A&A*, 423,65  
Kaastra J. S., 1992, *An X-ray Spectral Code for Optically Thin Plasma* (Internal Sron-Leiden Report, updated version 2.0)  
Liedahl D. A., Osterheld A. L., Goldstein W. H., 1995, *ApJ*, 438, L115  
Makishima K., Ezawa H., Fukuzawa Y., et al., 2001, *PASJ*, 53, 401  
Markevitch M., Forman W.R., Sarazin C.L., Vikhlinin, 1998, *ApJ*, 503, 77  
Matsushita K., Belsole E., Finoguenov A., et al., 2002, *A&A*, 386, 77  
McCarthy I. G., Balogh M. L., Babul A. et al., 2004, *ApJ*, 613, 811  
McWilliam A., 1997, *ARA&A*, 35, 503  
Mewe R., Gronenschild E. H. B. M., van den Oord G. H. J., 1985, *A&AS*, 62, 197  
Mewe R., Lemen J. R., and van den Oord G. H. J., 1986, *A&AS*, 65, 511  
Molendi S., Pizzolato F., 2001, *ApJ*, 560, 194  
Morrison R., McCammon D., 1983, *ApJ*, 270, 119  
Nulsen P. E. J., Böhringer H., 1995, *MNRAS*, 274, 1093  
Peres C. B., Fabian A. C., Edge A. C. et al., 1998, *MNRAS*, 298, 416  
Peterson J.R., Paerels F.B., Kaastra J.S., et al., 2001, *A&A*, 365, L104  
Pointecouteau E., Arnaud M., Kaastra J., de Plaa J., 2004, *A&A*, 423, 33  
Pratt G. W., Arnaud M., 2002, *A&A*, 394, 375  
Pratt G. W., Arnaud M., 2003, *A&A*, 408, 1  
Pratt G. W., Arnaud M., 2005, *A&A*, 429, 791  
Reiprich Thomas H., Böhringer H., 2002, *ApJ*, 567, 716  
Sanderson A. J. R., Ponman T. J., Finoguenov A. et al., 2003, *MNRAS*, 340, 989  
Sharma M., McNamara B. R., Nulsen P. E. J. et al., 2004, *ApJ*, 613, 180  
Snowden S. L. et al., 1997, *ApJ*, 485, 125  
Struble M. F., Rood H. J., 1999, *ApJS*, 125, 35  
Strüder L., Briel U., Dennerl K. et al., 2001, *A&A*, 365, L18  
Takahashi S., Yamashita K., 2003, *PASJ*, 55, 1105  
White D. A., Jones C., Forman W., 1997, *MNRAS*, 292, 419  
White D. A., 2000, *MNRAS*, 312, 663  
Yuan Q. R., Yan P. F., Yang Y. B., Zhou X., 2005, *ChJAA*, 5, 126